

Exploring the enhancement of infrared absorption through magnetically guided assembly of gold nanoparticle stabilized ferrofluid emulsion.

OKPOZO, P., DWIVEDI, Y., HUO, D. and PANCHOLI, K.

2023

This is the working paper / preprint version of the above paper. It was last revised on 27.01.2023

Exploring the Enhancement of Infrared Absorption through Magnetically Guided Assembly of Gold Nanoparticle Stabilized Ferrofluid Emulsion

Paul Okpozo¹, Yashashchandra Dwivedi², Dehong Huo³ and Ketan Pancholi^{1,4*}

¹School of Engineering, Sir Ian Wood Building, Robert Gordon University, Garthdee, Aberdeen, AB10 7GJ, UK

²Physics Department, National Institute of Technology Kurukshetra, Kurukshetra, 136119, India

³School of Engineering, Newcastle University, Newcastle, NE1 7RU, UK

⁴Advanced Materials Group, School of Engineering, Robert Gordon University, Aberdeen, UK

*Email: k.pancholi2@rgu.ac.uk

ABSTRACT

The molecular vibration signals were amplified by the gold strip gratings as a result of grating resonances and nearby electric field hotspots. Colloidal gold island films exhibit similar enhancement; however, the uneven geometrical characteristics of these films restrict the tunability of the vibrational enhancement. Infrared absorption is enhanced by regular metallic patterns such as arrays of strips fabricated using a top-down approach such as nanolithography, although this technology is expensive and difficult. The significant infrared absorption may serve as tunable antenna sensitization to improve the sensor performance. In this article, we present a simple one-step process for fabricating optically sensitive ordered arrays of a gold nanoparticle ferrofluid emulsion in polyvinyl alcohol (PVA) using a magnetic field and spin-coating directed self-assembly (MDSCSA) process. Techniques such as UV-visible absorption, scanning electron microscopy, and Grazing-angle Infrared spectroscopy were used to evaluate various parameters associated with the nanostructures. Unlike the gold strips, the chain-like features in the iron oxide nanoparticle arrays were discontinuous. The fabricated chain-like ordered arrays have been shown to increase the local field to enhance the infrared absorption corresponding to the symmetric vibration of the -CH₂ (2918cm⁻¹) group present in PVA by ~667% at 45° grazing angle of, as the chain thickness (CT) increased by 178%. This scalable and simple method can potentially generate low-cost patterns for antenna sensitization.

Keywords: Nanofabrication, Magnetism, Iron oxide, gold, thin film, Ferrofluid, Spin coating, FTIR, Pickering emulsion

1 INTRODUCTION

Infrared (IR) spectroscopy is a rapid, accurate, and remote method for the detection of molecules in a range of applications. For instance, its integration with microfluidics has enabled the detection of vascular endothelial growth factor (VEGF) for early disease diagnosis [1,2]. However, the sensitivity of IR spectroscopy is limited when detecting trace amounts of analytes, owing to the small cross-section of its molecular vibrational signals. Surface-enhanced infrared absorption spectroscopy (SEIRA) is commonly used to improve sensitivity. Metal nanostructures, such as gold gratings, have been found to be particularly useful in SEIRA, as the plasmon polariton resonance of gold gratings in the mid-IR region can be matched with molecular vibrational signals to enhance sensitivity. However, fabricating metal nanostructures with precise geometrical features requires slow, complex, and costly techniques such as gold sputtering, electron beam lithography, and nanoimprint lithography. To reduce cost and complexity and improve scalability, a simple, rapid, and less complex magnetically directed self-assembly technique (MDSA) can potentially be applied [3], [4]. Although MDSA can non-intrusively organize magnetic nanoparticles (NPs) to form arrays of chains [5], [6] suitable for applications in several fields such as photonics [7-9], storage devices [10], microfluidics [11,11(a)], and optical filters [12], it is difficult to organize poorly magnetic-responsive (diamagnetic) materials such as gold NPs. Combining non-magnetic and optically active materials with magnetic iron oxide helps overcome the limitations of MDSA and enables the formation of arrays of non-magnetic colloidal assemblies that are suitable for optical applications [13], [14], [15]. However, the irregular and jagged NP chains formed during MDSA processing, coupled with the presence of optically inactive iron oxide NPs, may not produce an optical response similar to that of the nanoimprinted gold strips. Additionally, controlling the film thickness produced using MDSA is not ideal. To address these challenges, in this work, the MDSA technique was modified and combined with spinning to form gold nanoparticle stabilised pickering ferrofluid emulsion chains to fabricate and study the feasibility of low-cost antenna for surface enhanced infrared absorption (SEIRA) spectroscopy. The modified MDSA technique, termed MDSCSA, helped to achieve long-range assemblies of gold NPs in the form of arrays of chains as the non-magnetic gold NPs adsorbed at the interfaces of the oil ferrofluid oil-in-PVA aqueous solution nanoemulsion droplets, also known as Pickering emulsions aligned to external magnetic field [16,16(a)], [17].

It is hypothesized that the clusters of gold and iron oxide NPs would help the electron transfer to enhance the local electric field, leading to an increase in the infrared-induced molecular vibrational signal [18], [19], [20] and also contribute to random light scattering [21] or interference [22], [23]. Because the interfacial interaction between gold and iron oxide causes the diffusion of the excited electrons from the Fermi level of gold NPs to the conduction band of the iron oxide, causing charge accumulation at the defect states of the interface [24][25], it is expected that the iron oxide in the ferrofluid droplet will interact with the adsorbed gold NPs and localize the electrons to increase the infrared molecular vibrational signal. Therefore, it is important to maintain the required concentration of gold NPs in the chains, the appropriate length and thickness of the chains, and gaps between chains. During magnetic directed self-assembly, the dipole-dipole interaction between magnetic particles or magnetic fluid droplets builds arrays of chain-like clusters that can span over a long distance at the microscale along the generated flux lines of the magnetic source [26], [27]. The density of these flux lines is dependent on both the size and strength of the magnetic field [28]; therefore, the chain length, thickness, and gaps between them can be controlled by suitably selecting the magnetic field strength, orientation, and distance from the subject. Additionally, these arrays of chains must be immobilized on the substrate, either by drying or curing an aqueous polymer [29], [30]. The composition considered in this study was an oil-based ferrofluid (hydrophobic phase) dispersed in polyvinyl alcohol (hydrophilic phase). This system tends to maintain the sphericity of the droplets and provides flexibility for the containing iron NPs to align and drive droplets to form chain arrays with respect to the magnetic field direction, as well as to maintain electrostatic, stearic, and viscous hindrance between droplets, preventing them from coalescing [31], [32].

The applied magnetic field can control the chain arrays and degree of orderliness; however, the introduction of spin coating contributes to the formation of thin-film mono-layered chain arrays. Spin coatings can also contribute to the rapid drying of most hydrophilic polymers [33], [34], [35], [36]. In this process, the contention between the magnetic force pulling the droplets towards the magnetic source and the inertial centrifugal hydrodynamic force of the fluid from the substrate spinning affects the distribution of the droplets and their chain clusters. Therefore, the process was optimized to control the chain morphology. This method allows the formation of a precise nanostructure that controls the plasmon excitation modes and shifts in infrared absorption at

different incidence angles of light. This outcome is useful for the development of sensitive biomedical sensors [37] [38], [39].

2 METHODS

2.1 Gold Nanoparticle Stabilised Pickering Ferrofluid Emulsion Preparation

As seen in Figure 1, oil-based ferrofluid [40],[41],[42] and gold methacrylate colloid were prepared (Supplement Data *S1.22.1* & *S.1.22.2*). Subsequently, the Polyethylene glycol-coated gold methacrylate (PEG-C-GM) nanoparticles were separated and dispersed in DI water. All materials and equipment are listed in *Supplement Data S1.21* & *S.1.21.1*. The prepared aqueous suspension of PEG-C-GM (4 mL) was dispersed in 20 mL of DI water in a sonicator bath for 5 min. Afterwards, 70 μ L of oil based ferrofluid was added, and the resulting mixture was stirred at 800 rpm using a rotor-stator for 8 min to create micron-sized emulsion droplets (~400 μ m diameter) of ferrofluid. Furthermore, it was irradiated for 10 min with trains of ultrasound pulses with a central frequency of 20 kHz using a probe-type sonicator, MSE® Soniprep 150, to reduce the diameter of the ferrofluid emulsion droplets. Each pulse duration was maintained at 10 s, while the transducer displacement was 10 μ m. The system was kept cool (~19 \pm 2° °C) by inserting it into a thermoregulating jacket. Six more batches were prepared using the same procedure. In order to reduce the degree of polydispersity, 15 milliliters of emulsion were centrifuged at a precisely determined speed of 1000 revolutions per minute for 10 minutes. Prior to determining the optimal speed and time of the size control process, a series of tests were conducted to optimize the size distribution. This nanoemulsion was termed polyethylene glycol-coated gold methacrylate Pickering ferrofluid (PEG-C-GM-pi-FF). This process is shown in the third row of Figure 1.

Separately, the 5 wt.%, 3.3 wt.%, 1.7 wt.%, 1.3 wt.% of aqueous PVA solution was prepared by adding PVA powder into DI water and stirred at 200 rpm for 10 minutes. The densities and viscosities of the resulting solutions with different concentrations are presented in Supplementary Data Table S-2. Subsequently, the solutions were heated at approximately 80 °C for 2.5 hours until they turned transparent. Five milliliters of the Pickering emulsion was then added to 10mL of an aqueous solution of PVA and stirred at 400 rpm for 1 h using a rotor

mixer.

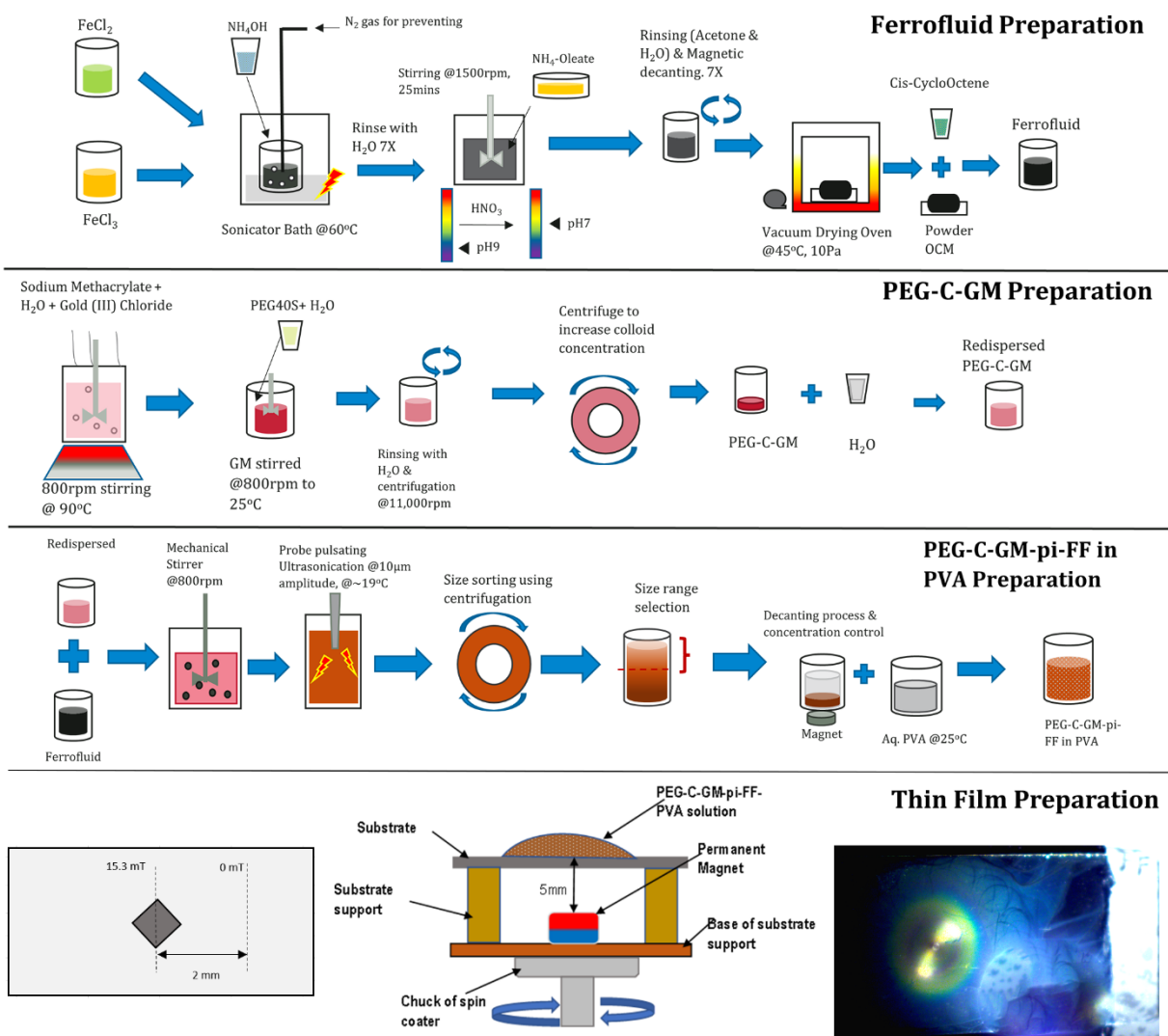


Figure 1: Schematic showing three stages of PEG-C-GM-pi-FF nanoemulsion manufacturing process and thin film preparation.

2.2 Gold Nanoparticle Stabilised Pickering Ferrofluid Emulsion Thin Film Preparation

To prepare a thin film containing arrays of chains of gold nanoparticle-stabilized Pickering ferrofluid droplets within an aqueous PVA solution, an experimental setup was designed, as shown in Figure 2(a), (b), and (d). Figure 2(b) shows the top-view and cross-section (Figure 2(b) and (d), respectively) views of the design. The magnet was placed approximately 5 mm below the surface of the substrate. A strong square shaped Neodymium magnet having 2.5 mm long edges and magnetic field strength of 202 mT on surface as measured by probe type gauss meter, was placed

beneath the surface of the substrate measuring 76.2 mm x 25.4 mm (Figure 2(b)). Figure 2(c) shows the magnetic field distribution across the substrate (mT).

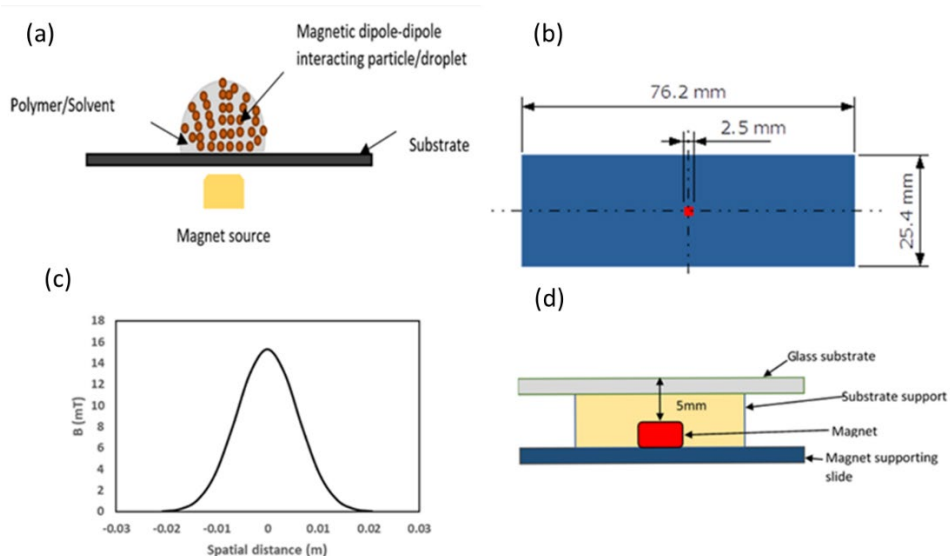


Figure 2: (a) Schematic representation of the magnetized droplet of gold nanoparticle-stabilized Pickering ferrofluid emulsion (PEG-C-GM-pi-FF) in an aqueous PVA solution. (b) Top view of the substrate with dimensions. (c) Measured spatial distribution of the magnetic field on glass substrate surface. (d) Cross-sectional view of the experimental setup used for measuring magnetic fields and preparing magnetic field-directed self-assembly of PEG-C-GM-pi-FF via spin coating. The glass slide supporting magnet is represented by the blue feature, and the magnet itself is depicted as a red square. The distance between the magnet and the glass substrate is 5mm.

The setup was spun using an SCS™ 6800 spin coater at a range of speeds programmed to operate within a specified timeframe. The spinner was set to spin at the maximum speed for 50s after 5s of acceleration. Finally, the spinner was decelerated for 5s to bring it to stand still and make it up to a total spinning time of 60s. These substrates were cleaned to remove debris on the surface with 70% w/w aqueous isopropanol solution and then dried in an oven at 60°C for one hour, especially for the glass slide. The effects of this treatment were tested using contact-angle measurements. Prior to the spinning process, PEG-C-GM-pi-FF (0.5 ml of PEG-C-GM-pi-FF in PVA solution) was allowed to settle on the substrate for 60 s, providing sufficient time for the droplets to interact with the magnetic field and build chain clusters. The thin-film coating was found to be dried only when it was spun at a speed above 700 rpm for 60 s, allowing the formed chains to immobilize on the substrate. After optimising the speed, viscosity and spinning time combinations, the array of

chains was prepared by spinning the substrate laden with PEG-C-GM-pi-FF (Viscosity of PVA solution used was 15.2mPas made from 3.3wt. %).

3 RESULTS AND ANALYSIS

3.1 Characterisation

3.1.1 Size Measurements

To increase the surface area and magnetic response to an external field, the ferrofluid was dispersed in a solution of oleic-coated magnetite (OCM) NPs with an average diameter of 15 ± 3 nm, as shown in the TEM image presented in *Figure 3(a)*. The oleic acid coating helped the NPs to remain stable without flocculation. The average hydrodynamic diameter of gold methacrylate (GM) and PEG-C-GM NPs determined using dynamic light scattering (DLS) was estimated to be 18.6 ± 3.9 nm and 28 ± 7.4 nm, respectively (Supplement data *Figure S2*), while the average mean diameter determined using TEM was estimated to be 17 ± 2.6 nm, as see in *Figure 3(b)* and 22 ± 4 nm, *Figure 3(c)*, respectively. The zwitterionic PEG molecules on the GM NPs enabled their adsorption on the ferrofluid droplets dispersed in the PVA aqueous solution, as can be seen in the TEM image (*Figure 3(d)*). In the TEM image, the PEG-C-GM NPs appeared as small dark particles on a large droplet of the ferrofluid. The average diameter of the PEG-C-GM-pi-FF emulsion measured using a Malvern zeta sizer showed a bimodal ferrofluid droplet size distribution with two peaks having central mean diameters of 610 ± 240 nm and 170 ± 16 nm (Supplementary *Figure S4*), respectively. PEG-C-GM-pi-FF droplets were subjected to centrifugal action to segregate larger droplets from smaller droplets within a specific time frame to narrow the entire size distribution. A total of 70,000 revolutions were required to attain a size distribution of $\sim 220\pm 50$ nm (see supplementary data, *Figure S5*).

3.1.2 Zeta potential

The attachment of methacrylic acid molecules led to an increased negative charge on the surface of gold nanoparticles, which was set at a value of -29.8 mV (*Supplementary Figure S3*), with a pH of 5.6, which is lower than that of gold-acrylic [43]. However, the zwitterionic PEG 40s coating reduced the charge on gold NPs by acting as a grafting layer [44]. The PEG-C-GM nanoparticle-

stabilized Pickering ferrofluid emulsion showed a lower electronegativity because of the low zeta potential of the ferrofluid in the PVA aqueous solution. Because the ferrofluid emulsion was only stabilized through the adsorption of gold nanoparticles, the overall charge was dependent on the number of NPs attached to the surface of the ferrofluid droplets [45]. However, the negative zeta potential of PEG-C-GM-pi-FF in the low-zeta potential PVA aqueous solution confirmed the adsorption of gold nanoparticles on the oil droplet. Moreover, the oil droplets were sufficiently large to reduce the overall surface area and zeta potential. The PEG coating as a layer of water-swollen gel generated supplementary steric repulsions between gold NPs [44]. Aqueous PVA showed low electronegativity, making it suitable to work with the Pickering emulsion, as two electronegative charges repel, thereby eliminating the possibility of chemical bonds forming that might distort the formation of droplet dipole-dipole chains upon the introduction of an external magnetic field. *Supplementary Figure S3* shows the zeta potentials of PEG-capped and uncapped gold methacrylate NPs with the zwitterionic characteristic of PEG effectively reducing the negatively charged layer on the gold particles.

3.1.3 UV-Visible Absorption Spectroscopy

The UV-visible absorption spectrum of 5 μ L of ferrofluid redispersed in 20 ml of *cis*-Cyclooctene was obtained. The resulting spectrum in *Figure 3(f)* matches that obtained in a previous report [46]. UV-visible absorption spectra were acquired for PEG-C-GM (*Figure 3(f)*). The surface plasmon vibration of colloids appears at 528 nm wavelength, which is characteristic of spherical AuNPs [43]. As seen in the *Figure 3(b)*, the prepared GM colloids showed a typical red color of gold [43][47]. The methacrylate ion adsorbed on the gold nanoparticles maintains the charge around the particles through hydrophobic-tail interactions, as shown in the schematic in *Figure 3(b)*, and prevents flocculation. The UV-visible absorption spectrum of the PEG-C-GM-pi-FF emulsion (*Figure 3(f)*) consisted of a broad absorption band spanning from range 515 nm to 610 nm. It is similar in terms of attaching gold nanoparticles to an iron oxide particle core, as presented in previous works [48] [49].

3.1.4 Thermal Gravimetric Analysis and Contact Angle

Thermal Gravimetric Analysis (TGA) revealed (see *Figure 3(g)*) that the thermal degradation of methacrylate on the GM surface was initiated at approximately 270°C and completed at 420°C,

°C showing a 6.5% loss of mass. For PEG-C-GM, an initial gentle decline in mass was observed between 30°C and 260°C °C before a steep decline up to 420°C, °C showing a total reduction in 12.8% mass. The concentration of methacrylate molecules was calculated and found to be 1.3×10^5 molecules (see Supplementary Data (SI.13) for the calculation step) [50]. Images of the droplets for different PVA concentrations were analyzed using the contact angle plugin of ImageJ® software [51]. The contact angle between the glass slide and the PVA droplet increased with increasing PVA concentration (Supplementary Figure S6(c)). A typical image in Supplementary Figure S6 (a&b) shows the contact angle of 16.9° for 3.3w/w % solution confirming the good adhesion of PVA solution with the substrate. The interfacial tension between PEG-C-GM-pi-FF and the glass slide in DI water based on the (LBADSA) plug-in of Image J® [52] gave a contact angle of 174.88°. The image scale was set to $316 \times \text{mm}$ (Figure 3(g)).

3.1.5 Magnetic Hysteresis

A superconducting quantum interference device (SQUID) was used to measure the magnetic moments. As seen in the *Supplementary Figure SI(A)*, the saturation of magnetization (M_d) for bulk Fe_3O_4 is 446 kA/m, and the saturation of magnetisation M_s for Fe_3O_4 and OCM nanoparticles are 374.8 kA/m and 219.9 kA/m, respectively. The magnetic susceptibility X_{iL} , which is the initial slope of the curve intercepting at zero magnetic field for Fe_3O_4 and OCM, is 8.6 and 1.5, respectively. The coercivity of Fe_3O_4 nanoparticles and OCM from *Supplementary Figures SI(B&C)* are 1.8 kA/m and 1.3 kA/m respectively. The obtained experimental data were used to determine the effective diameter and standard deviation of the tested materials using the model [53] [54] (see Supplementary Data SI.9)

The effective diameter of 13.7 ± 2.94 nm estimated using this method, was similar in terms of the diameter and standard deviation obtained from the TEM micrograph of OCM in *Figure 3(a)*. The difference between the estimated diameters obtained using the two methods could have been due to the coating layer (oleic acid), which reduced the effective magnetization of magnetite (Fe_3O_4). The estimated diameter (14 ± 3 nm) of the magnetite NPs, on the other hand, was much closer to the average diameter obtained by TEM micrograph. The saturation of magnetization for the ferrofluid (OCM dispersed in *cis*-Cyclooctene) obtained was 29.5 kA/m. This gave a magnetization ratio between the OCM particles and ferrofluid of 0.06.

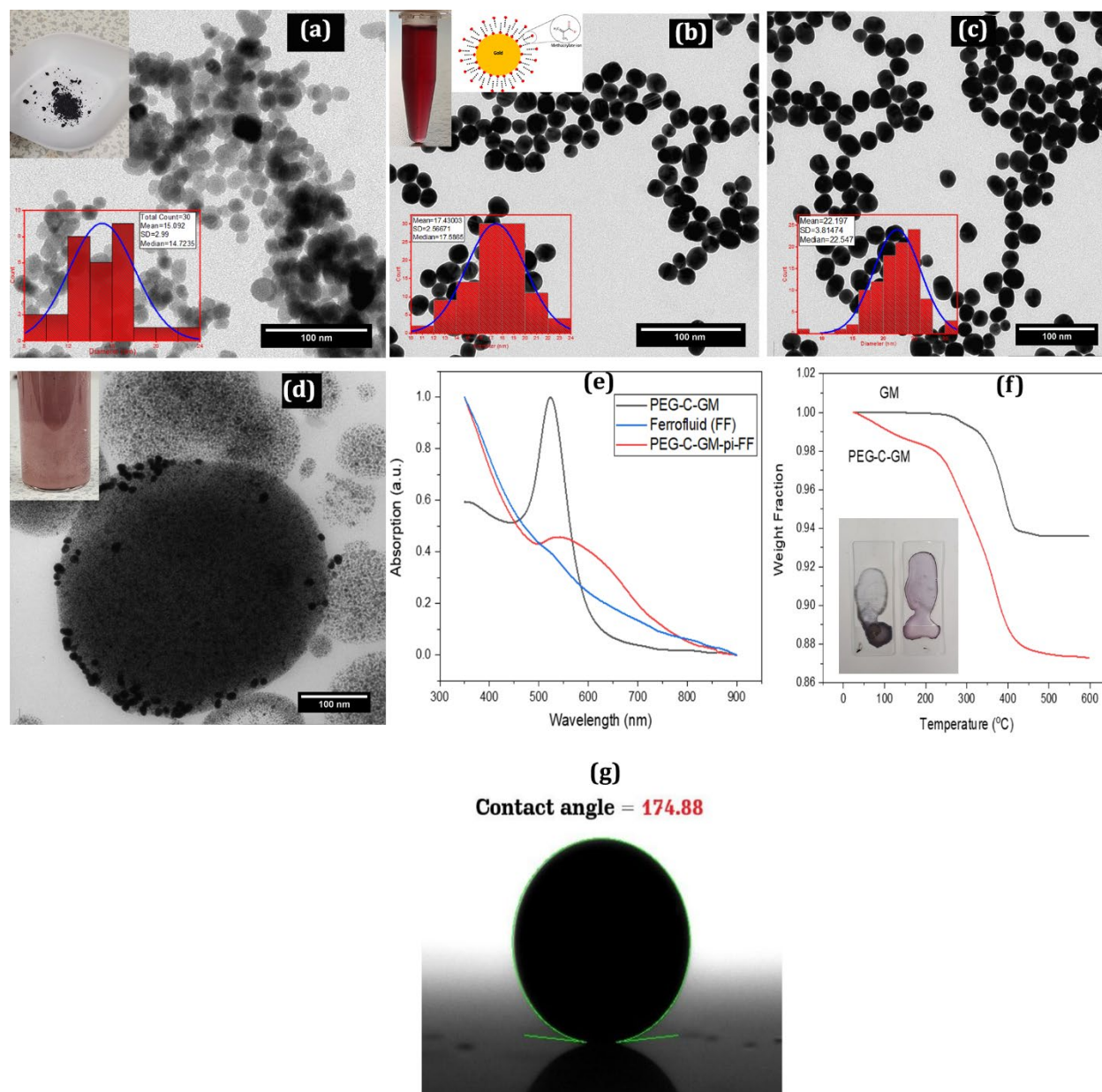


Figure 3: Characterization of colloids, nanoparticles, suspensions, and emulsions prepared using Transmission Electron Microscopy (TEM), contact angle measurements, UV-Vis absorption, and Thermogravimetric Analysis (TGA)

(a) TEM image of prepared Fe_3O_4 nanoparticles, with an inset showing the size distribution (mean size of ~ 15 nm and a standard deviation of 2.99 nm). (b) Size distribution of gold methacrylate (GM) nanoparticles with a mean size of ~ 17 nm and a standard deviation of 2.57 nm, with an inset showing an image of the wine-coloured GM solution and methacrylate chains illustration. (c) PEG-coated Gold Methacrylate nanoparticles, with an inset showing the size distribution (mean size of ~ 22 nm and a standard deviation of 3.8 nm). (d) Dried PEG-C-GM-pi-FF droplet. (e) UV-Vis spectra of PEG-C-GM, ferrofluid and PEG-C-GM-pi-FF. (f) TGA of GM and PEG-C-GM, with an inset showing the colour of dried droplets. (g) The contact angle (174.9°) for ferrofluid droplets in PEG-C-GM solutions, obtained using Low Bond Axisymmetric Drop Shape Analysis (LBADSA) plug-in of Image J[®].

3.1.6 Fourier Transform Infrared Spectroscopy

The Fourier Transform Infrared (FTIR) spectra of all prepared colloids, emulsions, and individual materials were measured (see Supplementary Data *SI.15*) to identify and monitor the changes in molecular vibrations affected by mixing various components or due to interactions between individual components during the synthesis process.

3.1.6.1 Gold Methacrylate (GM), Oleic Coated Magnetite (OCM) and Ferrofluid (FF)

The FTIR spectra for oleic acid-coated Fe₃O₄ (OCM) are presented in both *Figure S 6 (A-2)* while the spectra of each component of the ferrofluid, such as oleic acid(OA) (*Figure S-6(A) – 1*), *cis*-Cyclooctene (*Figure S-6(A) – 3*), and ferrofluid-(FF), *Figure S-6(A) – 4*) are also presented in the respective images.

On the surface of the OCM NPs, a decrease in the absorption peaks for the CH₂ symmetric and asymmetric stretch vibrations (2849 cm⁻¹ and 2918 cm⁻¹) corresponding to oleic acid was observed, confirming the successful binding to the surface of the Fe₃O₄ NPs (Supplementary Data *Figure S-6(A) – 1&2*). Two new bands appeared at 1595 cm⁻¹ and 1541 cm⁻¹, corresponding to the symmetric and asymmetric stretching of COO⁻, respectively, which indicate attachment to the ferrite surface. These vibrations are small but visible, confirming their interaction with the iron oxide NPs. [55] [56] [57]. The spectrum of the ferrofluid (*Figure S-6(A) – 4*) is dominated by *cis*-Cyclooctane vibrations, which buried the other molecular vibrations, while the Fe-O stretching vibration at 567 cm⁻¹ is still visible (*Figure S 6 (A) – vi*) [58]. The other bands are presented in Supplementary data *Table S-4*.

The methacrylate molecules capped the gold methacrylate surface layer via the CH₂(~1360 cm⁻¹) group (*Figure S-6(B)-4*). Furthermore, the carboxylic end points outward, causing the nanoparticles to repel under the effect of electrostatic charges on the surface layer [59]. The FTIR spectrum of GM was similar to that of silver-capped poly (methyl methacrylate) [60], with a broad band of O-H stretching appearing at 3327 cm⁻¹ (*Figure S-6(B)-2*). The bands in the range of 1700 – 1711 cm⁻¹ assigned to C=O (*Figure S-6(B)-3*) stretching conjugated acid signify freely attached methacrylic acid [61]. The C=C stretching conjugated alkene appeared at 1647 cm⁻¹ while the bands at 1454 and 1393 cm⁻¹ were assigned to the asymmetrical and symmetrical bending

vibrations of the methyl group [62]. The O-H bending vibration of the PEG added to cap the particle appeared at 1411 cm^{-1} while the band in the range of $1240 - 1107\text{ cm}^{-1}$ (*Figure S-6(B)-5*) was assigned to C-O stretching alkyl aryl ether. The C-O stretching vibrations of the secondary alcohol of PEG and vinyl ether appeared at 1101 and 1205 cm^{-1} , respectively, which disappeared for the PEG-capped particles. Band at 836 cm^{-1} in (*Figure S-6(B)-6*) is assigned to the bending alkene of the methacrylate molecule [62]. The spectrum of gold methacrylate was similar to that reported elsewhere [63][64]. However, the intensity of GM vibrations was significantly suppressed in the PEG-C-GM IR spectrum. The other bands are listed in Supplementary *Table S4*.

3.1.6.2 PEG-C-GM-pi-FF-PVA

The FTIR spectra of the final mixtures are shown in both *Figure S-5 (C)*;PVA and the corresponding mixtures in PVA, such as PEG-C-GM-pi-FF (*Figure S-5(C)-1*), PVA (*Figure S-5(C)-2*), PEG-C-GM-PVA(*Figure S-5(C)-3*), FF in PVA(*Figure S-5(C)-4*), and PEG-C-GM-pi-FF-PVA(*Figure S-5(C)-5*). PEG-C-GM Pickering reduced the molecular vibrations of the ferrofluid (*Figure S-5(C)-1*). It is expected that the droplet was potentially densely covered by the gold NPs, which suppressed the vibrations. The spectrum (see *Figure S-5(C)-2*) of PEG-C-GM-pi-FF-PVA showed the dominant peak of $\text{CH}_2(2847\text{ cm}^{-1})$ corresponding to PVA, which was not observed in the other peaks related to FF and GM. In the case of the FF in the PVA spectra, an amalgam of vibrations due to cyclooctane and PVA appeared, which altered the transmittance. This was not observed with PEG-C-GM-pi-FF, which exhibited very similar transmittance spectra to that of PEG-C-GM-PVA, yet confirmed the interfacial coverage by PEG-C-GM on FF. The other bands are presented in Supplementary *Table S4*.

3.2 Morphology of Spin Coated Samples

MSCDS processing of PEG-C-GM-pi-FF-PVA yielded a thin film on a glass slide, as shown in *Figure 4(a)*. Optical and scanning electron microscopy of the thin film showed arrays of parallel chains of PEG-C-GM-pi-FF on the substrate with varying spatial densities. Therefore, the image shown in *Figure 4(a)* was divided into three regions. A typical dark-field image of the thin film (Region 2) coated with PEG-C-GM-pi-FF-PVA is shown in *Figure 4(b)*.

In all cases, drying started from the outer edges of the substrate and was directed inward, generating a circular pattern whose diameter decreased with increasing spinning time. The film in

the region of interest was divided into three regions, as shown in *Figure 4(a)*.

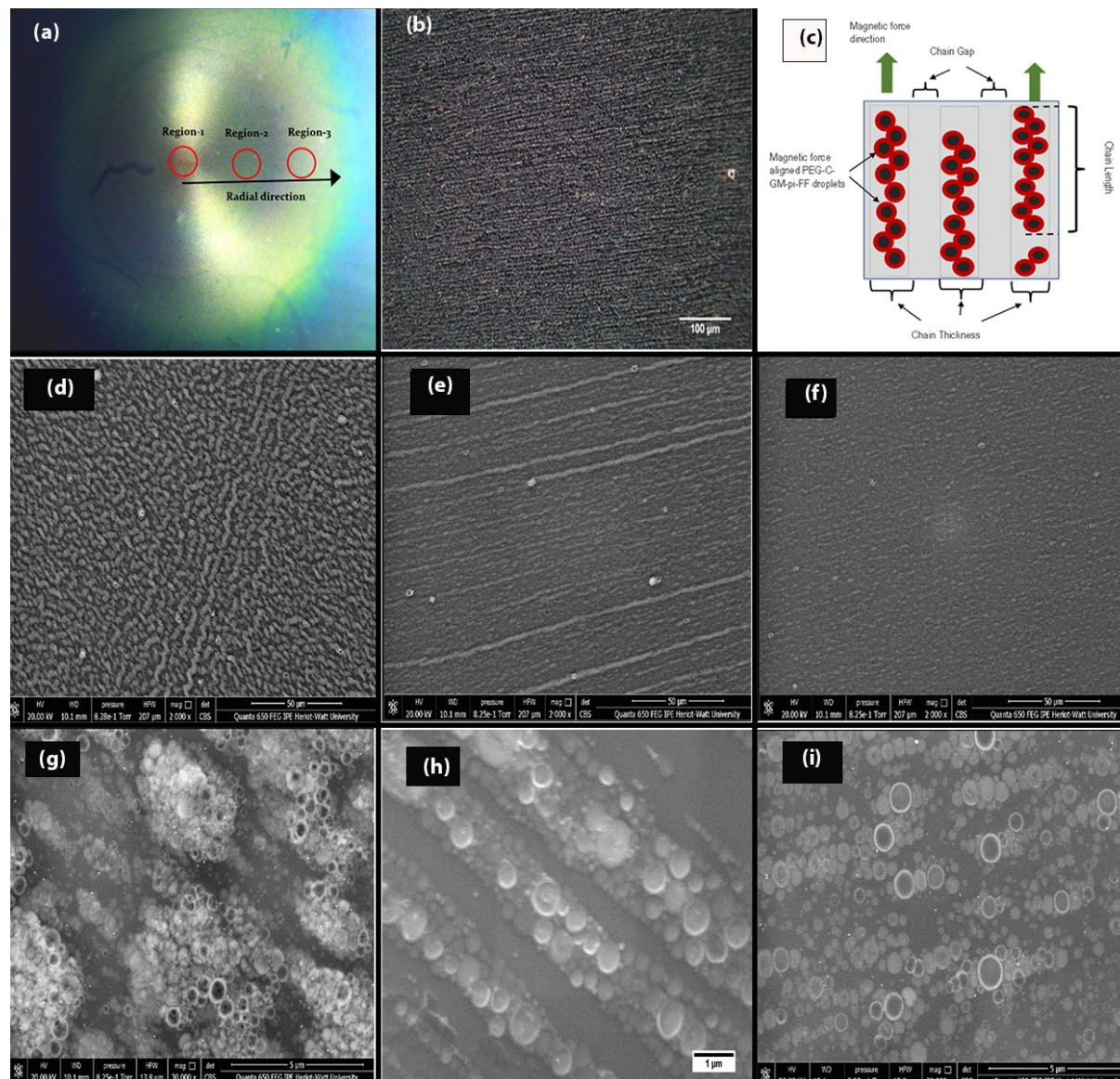


Figure 4 (a) shows a PEG-C-GM-pi-FF-PVA thin film on a glass slide prepared using MSCDS. The film is divided into three regions, labelled Region 1 ($r=0\text{mm}$), Region 2 ($r=4\text{mm}$), and Region 3 ($r=7\text{mm}$), where " r " represents the radial location in millimetres from the centre of the film where the magnet was located. *Figure 4 (b)* is an example of a dark field image of arrays of PEG-C-GM-pi-FF obtained using an Olympus BX41 microscope with a 20X 0.4 N.A. M-Plan objective lens. *Figure 4(c)* illustrates the 1D pattern morphology, showing chain length (CL), chain thickness (CT), and chain gap (CG). *Figure 4(d & g)* are scanning electron microscope (SEM) images of the thin film at the centre of the substrate ($r=0\text{mm}$) at various resolutions (resolution 17 pixels and 1820 per μm , respectively), showing dense clusters of PEG-C-GM-pi-FF. *Figure 4 (e & h)* are SEM images of the thin film at $r=4\text{mm}$, displaying longer chain structures with an average of 4 droplets thickness, (resolution 17 pixels and 1820 per μm , respectively). Lastly, *Figure 4 (f & i)* are SEM images of the thin film at $r=7\text{mm}$, showing shorter chains with a maximum of 2 droplets thickness (resolution 17 pixels and 1820 per μm , respectively).

Figure 4(g)& (h) and *(i)* show the corresponding chain arrays at higher resolution (1820 pixels/ μm), where emulsion droplets are visible with white rings appearing as corona of the adsorbed gold nanoparticles at the circumference. Because of the high magnetic strength at the

center of the magnet, thicker columns with worm-like or labyrinth-like formats were established. The chain length (CL) of PEG-C-GM-pi-FF was found to be shorter and densely packed at the center ((*Figure 4(d)*) of the film, but it increased in length at a location away from the center (*Figure 4(e)*). However, chain formation was no longer visible at a location far away from the center of the rotation of the film in the SEM image (*Figure 4(f)*), and that location was not included in the image analysis. These chains were separated by a small or negligible gap. To formalize the geometrical features of these chains on the substrate, the chain gap (CG), chain length (CL), and chain thickness (CT) are defined in *Figure 4(c)*. Some thin-film nanostructures possess two-fold symmetries, which indicates long-range ordering of particles [65]. CL, CT, and CG were quantified using image analysis to estimate the effect of the geometrical features of the patterned thin film. Further details related to the image analysis are provided in *Supplement Data S1. 17* and *S-1.18*.

3.3 UV-Visible Absorption of Thin Film

The UV-visible absorption spectrum was obtained for each location ($r=0, 2, 4,$ and 7 mm from the center, associated with CT/CG ratios of 2.87,0.97,0.73 and 0.07, respectively) on the thin film (*Figure 5(a)*). The obtained broadband spectra were deconvolved using a multi-peak nonlinear Gaussian fitting model in the Origin® software (details in *Supplementary S 1.19*). Each spectrum appears as a broadband absorption spectrum with one or two prominent peaks at both ends of the spectrum (~ 444 nm and ~ 680 nm), along with undulating peaks between them. As shown in *Figure 5(a)*, the absorbance observed at the center of the film ($r=0$ mm) is greater than 1, which can be attributed to the high density of droplets present in that area. These droplets cause incoherent scattering and multiple reflections of the light waves, leading to increased absorption.

The peaks observed in *Figure 5 (a)* are consistent with those observed in the spectra obtained from structures in which gold nanoparticles were embedded within an iron oxide layer or laid on the surface, as reported in previous studies (*Table-1*) [68]. The UV-Vis results showed the interaction between the iron oxide NPs and gold NPs. These interactions established SPR, even in the presence of iron oxide NPs.

As depicted in *Figure 5 (a)* and *(b)*, the band at 480 nm (Band-C) could be attributed to the spin-flip Fe-Fe pair transition in the iron oxide structure (3^{rd} row, *Table 1*) [69,70]. The intensity and

absorption wavelength of this band depend on the size and/or shape of the iron oxide particles [71]. The absorption bands between wavelengths 400 nm and 500 nm are associated with iron oxide absorption. The two distinct absorption bands in the resulting spectra at ~ 444 nm (Band-A) and ~ 680 nm (Band-F) were associated with Fe_3O_4 [66] and red-shifted plasmon resonance of gold NPs, respectively. Iron oxide and gold did not develop into bimetallic nanoparticles, as previously noted [67], because the dimer (iron oxide and gold) generated in the thin-film nanostructure was not created by the thermal process. Instead, the structure resembled gold particles embedded in the iron oxide layer.

Within the 500–650 nm spectral range, the two absorption peaks at ~550 nm (Band-D) and ~630 nm (Band-E) were attributed to the interaction between the iron oxide and gold nanoparticles on the dielectric surface of silicon glass. This interaction is caused by frequency-oscillation coupling from small interfacial contacts, as reported in previous studies [68, 71, 72]. As a result, this interaction leads to a red shift in the plasmon resonance of gold from its non-interacting plasmon mode (~520 nm) to ~550 nm, depending on the degree of interaction, similar to the red shift observed for gold-silica nanostructures [73-77]. Furthermore, this shift can also be observed through an increase in the density of gold nanoparticle aggregates and a reduction in interparticle/chain spacing. The intensity of the 550 nm peak was weak at a radial distance of $r = 7$ mm. This is expected as the volume fraction of gold nanoparticles per unit area decreases and the interparticle spacing increases, resulting in a significant reduction in the plasmonic red-shift [78-80]. As shown in Figure 5 (a), the absorbance between 444 and 550 nm was found to be twice that of the spectrum obtained from the location at $r=7$ mm. However, the overall absorbance as well as the peak absorbance (in the 440–560 nm range) were observed to decrease in the spectrum obtained from locations farther from the center of the film. The absorption spectra at $r=0, 2, 4,$ and 7 mm (Figure 5 (a) and (b)) showed a weak absorption peak at ~517 nm, which is attributed to uncoupled or dislodged gold nanoparticle (dis-Gold) plasmonic resonance.

Moreover, the high concentration of gold NPs at the interface provided condition to generate an SPR peak at 517 nm. (see Fig. 5 (b)). The visible distinctive peaks can be attributed to the grating structure and increased absorbance due to surface resonance.

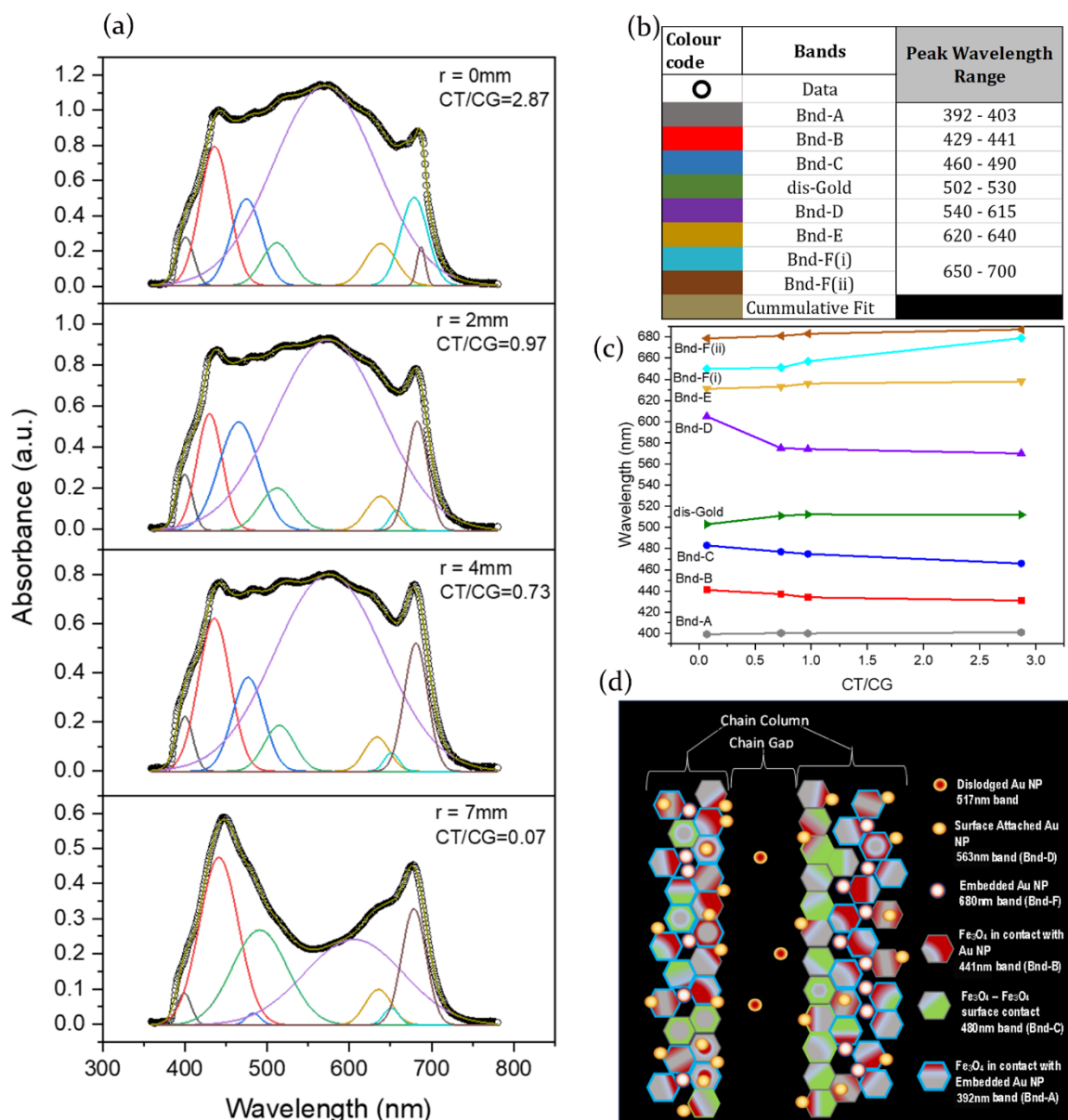


Figure 5 presents UV-Vis spectra for a thin film. Panel (a) displays the deconvoluted UV-Visible absorption spectra of thin film locations ($r=0, 2, 4$ & 7 mm), with fitting bands (Bnd). Panel (b) includes a legend showing colour assigned to each band (Bnd) shown in panel (a) and their respective peak wavelength range. Panel (c) shows the peak wavelength shifts of each band (Bnd) corresponding to every CT/CG ratio, indicating the dependence of photo-absorption of gold and Fe_3O_4 resulting from charge transfer dynamics on the thickness of chains and gaps between chains. Detailed results can be found in supplementary S1.19. Panel (d) includes a schematic illustration of particle-particle interaction and charge transfer within a PEG-C-GM-pi-FF chain, with added captions describing the expected absorption bands associated with gold NPs and various states of interactions between gold and Fe_3O_4 NPs.

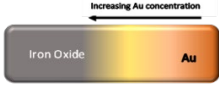
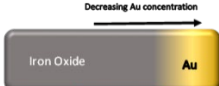
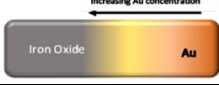
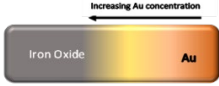
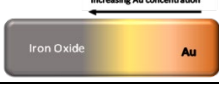
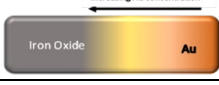
At a radial distance of $r=0$ mm, the peak intensity (~ 1.18) for Band-D (~ 550 nm) correlated with the highest values of CT and the lowest values of CG. A blue shift of 20 nm was observed when the CT/CG ratio was increased from 0.07 0.73. This blueshift suggests that the increased energy

contributes to the nonlinear optical effect. The 517 nm band was observed at radial distances ranging from $r=0$ to 4 mm, which is attributed to a higher concentration of gold nanoparticles per unit area, resulting in the generation of surface plasmon resonance (SPR). The thick chains (with a CT/CG ratio ranging from 2.87 to 0.73) exhibited a higher concentration of adsorbed gold nanoparticles (NPs) and a reduced interparticle spacing in comparison to the locations where the CT/CG ratio was 0.07, likely due to the presence of a higher number of ferrofluid Pickering emulsion droplets.

As the CT/CG ratio increased at the observed locations on the thin film, a blueshift for Band-B and Band-C was observed as the cumulative charge transfer across the interfaces between iron oxide and gold nanoparticles established within a chain cluster. The blue-shift of Band-B in this region of the substrate resulted from an increase in the iron oxide concentration in relation to the gold nanoparticles. Band C is a band that results from the interaction between iron oxide and iron oxide. This was initially hardly visible in the UV-visible absorption spectra but was clearly visible when gold nanoparticles were introduced. Therefore, it is safe to assume that Band-C emits from iron oxide-iron oxides, which are in close proximity to gold NPs (see *Figure 5 (b)*)[71]. A red shift and decrease in the intensity of Band-F indicate a reduction in gold concentration, leading to a redshift as CT/CG decreased [81][82]. At $r=7$ mm, the 550 nm peak disappeared because of the decrease in the gold concentration. Band E appeared red-shifted with decreasing peak intensity. This trend results due to average decrement of gold-iron oxide interaction ratio, where more gold was located at the center of the sample and decreasing as ' r ' increases.

Except for vibration bands A and F, the other vibrations (Band-B and Band-C) appeared to be sensitive to the concentration ratio of iron oxide and gold, and the size of the cluster chains, resulting in frequency shifts, absorption intensity, or bandwidth. In the embedded configuration[68], where gold NPs were embedded in a ferromagnetic film, the peak plasmon resonance appeared at a longer wavelength (> 630 nm), indicating a low mismatch in frequencies between the coupling of the oscillators in the iron oxide (ferromagnetic) NPs and gold NPs. If the gold NPs were on the surface of the iron oxide NP film (surface configuration), the small interfacial contact area between iron oxide and gold led to frequency oscillation matching of gold plasmon absorbance and iron oxide band gap absorbance at approximately 550 nm. Interestingly, the patterned PEG thin film of PEG-

Table 1: Summary of the absorption bands occurs in PEG-C-GM and Fe₃O₄ nanoparticle configurations.

Bands		Configuration	Assumed Gold-iron oxide concentration	Band behaviour (Red-shift= RS , Blue-shift= BS , Band broadening= BB , Band narrowing= BN . Peak intensity: decrease= \downarrow , increase= \uparrow)	Reference
Band-A	400nm	Embedded		BS , \uparrow , BN	[69]
				RS , \downarrow , BB	
Band-B	444nm	Surface		RS , \uparrow , BB	[67] [84]
				BS , \downarrow , BN	
Band-C	480nm	Fe-Fe quantity	Decrease in CT_w	RS , \downarrow , BN	[71] [74]
			Increase in CT_w	BS , \uparrow , BB	
Band-D	550nm	Surface		BS , \uparrow , BB	[69] [71] [72]
				RS , \downarrow , BN	
Band-E	630nm	Embedded/ Surface		BS , \uparrow , BB	[81] [68] [81]
				RS , \downarrow , BN	
Band-F	680nm	Embedded		BS , \uparrow , BN	[68] [69]
				RS , \downarrow , BB	

C-GM-pi-FF can be considered a multifaceted configuration of “embedded” and “surface” types. In the middle of the chain, the gold NPs were trapped within the iron oxide cluster chains and, therefore, had a large surface area of interaction, leading to a peak at longer wavelengths. On the surface of the PEG-C-GM-pi-FF chains, the adsorbed AuNPs were responsible for the peak at 550 nm. Therefore, a broadband spectrum was observed owing to the combination of the two

configurations. Table 1 shows a summary of the impact of the iron oxide-gold interaction and variation in peaks. Such observations, therefore, confirmed the hypothesis opposing the concept of electron diffusion from gold nanoparticles to iron oxide, instead of the increase in electron density at their interface [83]. This electron density at the interface bends the conduction band of iron oxide, thereby improving its optical response in the form of an increase in photo-absorption. Parameters such as configuration, degree of interaction, and concentration ratio of gold and iron oxide strongly influenced the absorption peaks within the broadband spectrum.

3.4 Surface Enhanced Infrared Spectroscopy

In a previous study, the SR-FTIR technique was employed to observe the local field enhancement created by the nano-printed gold grating under varying degrees of incidence angle of the infra-red beam [84]. When the grating period of the gold strip deposited on substrate was closer to the CH₂ (asymmetric and symmetric) vibrational excitation bands of the molecules (of coated layer of Mercaptohexadecanoic acid), the absorbance in their investigation was shown increased by a factor of 6000. Similar observations were made for PMMA molecules adsorbed on regular gold grit [85]. A specific collection of vibrational bands with frequencies near the grating diffraction size was affected by the gold strip pattern dimensions, in addition to being responsible for local amplification. In this work, chains of iron oxide and gold NPs were created and analyzed using UV-Vis spectroscopy. In the UV-Vis results, the interaction between iron oxide and gold NPs leading to SPR was observed. However, the effect of the pattern dimension (chain thickness and gaps) of the fabricated thin film on the IR absorption of molecules in PVA has not been established. Specular reflectance Fourier Transform infrared (SR-FTIR) spectroscopy was performed at angles of 45°, 20°, and 82° °to observe the surface-enhanced infrared signals from the PVA adsorbed on the PEG-C-GM-pi-FF arrays in thin film (prepared using 15.2mP as viscosity solution at a spin speed of 2500rpm). See *Supplementary Data SI.8* for the description of the method.

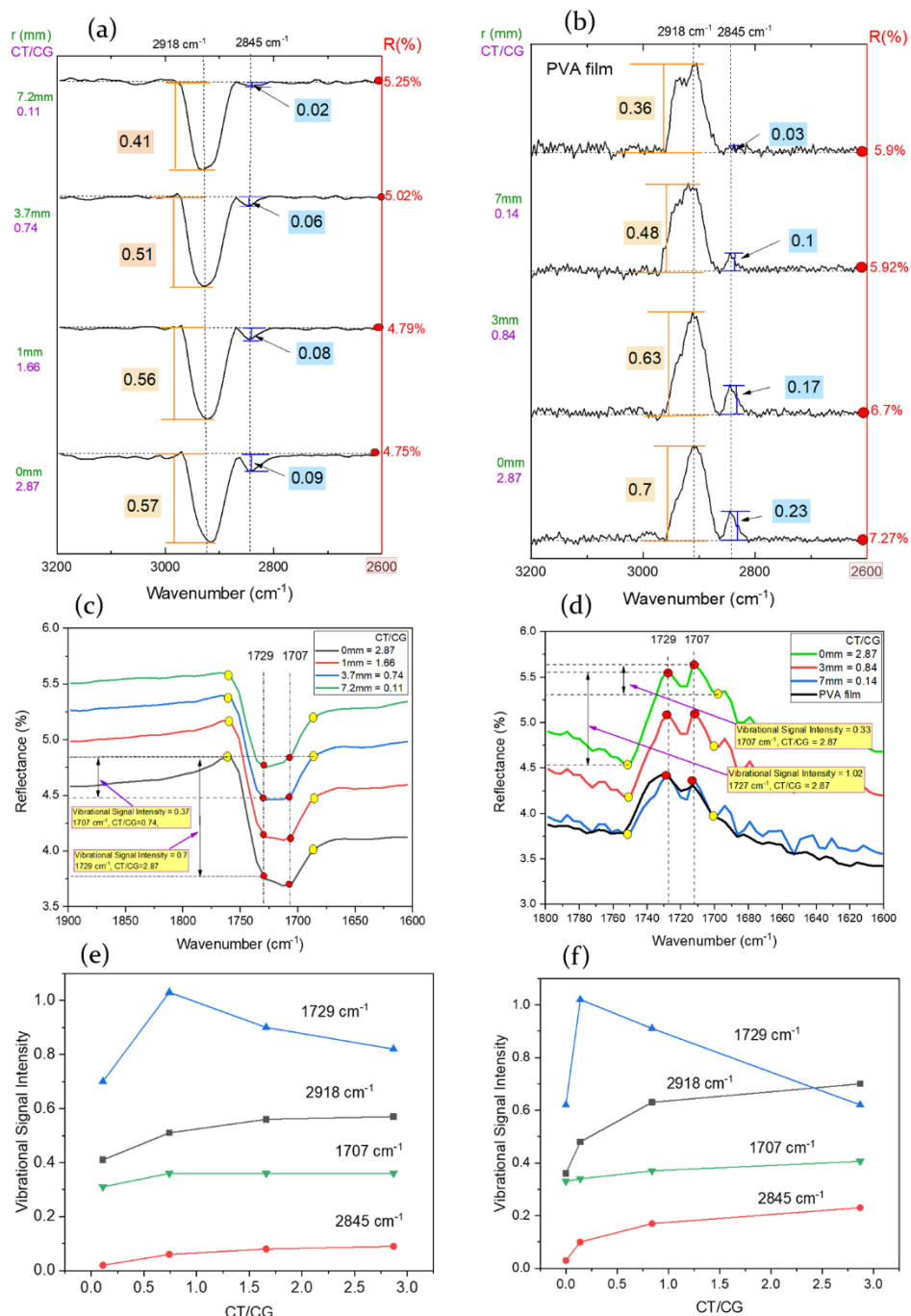


Figure 5: The figure presents the results of specular reflectance FTIR spectroscopy of PEG-C-GM-pi-FF chains on a glass slide at different radial distances from the centre of the thin film, where a magnet was placed. The CT/CG ratio is highest at the centre of the film ($r=0\text{mm}$) and lowest at the outermost location on the film ($r=7.2\text{mm}$). Plots (a) and (b) display the variation in the signal intensity of the -CH bond vibrations (2918cm^{-1} and 2845cm^{-1}) at grazing angles of 20° and 45° , respectively, with 2600cm^{-1} used as the reference reflectance intensity point ($R\%$). Plots (c) and (d) depict the change in vibrational intensity of the CO bond (1729cm^{-1} and 1707cm^{-1}) at grazing angles of 20° and 45° . Plots (e) and (f) illustrate the relationship between the intensity of vibrational peaks and the CT/CG values at grazing angles of 20° and 45° degrees, respectively.

The FTIR spectra at angles of incidence (20° and 45°) are shown in *Figure 6* for the range of 4000cm^{-1} to 650cm^{-1} . The 82° incidence angle is shown in Supplementary (*Figure S-9*). The entire spectrum was split into two parts: the first having a range of 3200cm^{-1} to 2600cm^{-1} , and the second having 1900cm^{-1} to 1600cm^{-1} .

3.4.1.1 Range 3200cm^{-1} to 2600cm^{-1}

As shown in *Supplementary Figure S7*, the broad absorption band at $3600 - 3000\text{cm}^{-1}$ is associated with the OH stretching vibrations in PVA molecules, whereas the vibration between $2923 - 2900\text{cm}^{-1}$ is attributed to the asymmetric stretching of the methylene (C-H) group in the prepared arrays of PEG-C-GM-pi-FF chains on the glass substrate[86][87]. The intensity of the symmetric stretching vibrational mode at 2846cm^{-1} associated with the methylene group [88] was found to increase relative to the asymmetric vibrational intensity ($\sim 2918\text{cm}^{-1}$) at shorter radial distances (CT/CG = 1.66 at 20° grazing angle and CT/CG = 0.84 at 45° grazing angle, (see *Figure 6* (a) and (b), respectively)) from the center of the thin film. Previous reports suggest that the increase in vibrations (2918cm^{-1} and 2845cm^{-1}) of the PVA gold composite is related to an increase in the gold NPs concentration [89]. However, the interface between gold NPs and iron oxide NPs in the proximity of the arrays of GSPFE chains potentially enhances the electromagnetic field throughout the PEG-C-GM-pi-FF film [90]. Therefore, the observed increase in the methylene vibrational mode intensities reflected the increase in gold concentration and, thus, the increase in the gold/iron NPs interface. The increase in the CT/CG ratio also correlated with the increase in gold-iron oxide NP interfaces; therefore, the various vibrational mode intensities are further discussed in Section 3.3.1.3. Bulk PVA has vibration modes at $\sim 2918\text{cm}^{-1}$ and 2845cm^{-1} corresponding to PVA-CH-asymmetric and PVA-CH-symmetric vibrations, respectively.

3.4.1.2 1900cm^{-1} to 1600cm^{-1}

As seen in *Figures 6* (c) and (d), the 1367cm^{-1} and 1409cm^{-1} vibrational modes associated with -OH bending in C-H wagging or -CH₃ stretching and C-H deformation, respectively, were observed in the FTIR spectrum of the PEG-C-GM-pi-FF chain arrays in PVA. The observed vibrational mode at 1707cm^{-1} could be associated with C=O vibrations [87][88], and the $\sim 1729\text{cm}^{-1}$ mode was ascribed to C=O vibration due to the presence of acetate molecules within the PVA (88% hydrolyzed) [91]. It can be observed that at scan locations closest to the middle of the substrate, a relative increase in the CA-CO (1707cm^{-1}) vibrational mode intensity compared to PVA-CO

(1729 cm^{-1}) was observed, whereas at further scan points away from the center, the reverse was observed. The vibration signal difference was related to the chain thickness-chain gap ratio (CT/CG) and chain thickness (CT) for angles of incidence of -20° and 45° . The spectra for the 82° angle are presented in *Supplementary Data (S1.20)*.

3.4.1.3 Surface Morphology dependent Enhanced Infrared Absorption

The same locations of the films of PEG-C-GM-pi-FF were used to acquire the FTIR spectra and optical images, and the spectra were matched with the CT/CG values obtained from image analysis of a $50 \mu\text{m}^2$ scan area (**Table S8**). As seen in *Figure 6(a,b,c&d)*, the vibrational mode intensities of the local minima points (yellow circles) were subtracted from the maximum vibrational mode intensities (red circles) associated with each spectral position to determine the surface-enhanced absorption signals. Subsequently, the obtained vibrational signals correlated with each CT/CG ratio (*Figure 6e&f*). It must be noted that the corresponding values of $r(\text{mm})$, $\text{CT}(\mu\text{m})$, and CT/CG were correlated (see **Table S8**); therefore, these terms are used interchangeably in the Discussion section.

The relationship between CT/CG and the vibrational signals of PVA-CH-symmetric and PVA-CH-asymmetric was found to be nonlinear at all angles of incidence (20° , 45°). The -C-H asymmetric and symmetric vibration resonance modes ascribed to the methylene group present in PVA were of the same intensity as those at $r=7 \text{ mm}$ (*Figure 6a&b*). At 20° incidence, the vibration signals of the -PVA-CH-asymmetric band increased with the CT/CG ratio (*Figure 6e*). A gentle increase in vibrational intensity up to the highest CT/CG ratio at 2845cm^{-1} was observed. The PVA-CH-symmetric and asymmetric vibrational signals increased by 350% and 39%, respectively, with an increase in the CT/CG ratio of 170%, and a similar increasing trend for chain thickness (**Table 2**) was also observed. The charge interaction between iron oxide-gold NPs would have increased with an increase in the CT/CG values, as observed in the UV-visible absorption spectra. The increased charge transfer at high CT/CG values may have increased the vibrational signals. The combination of embedded and surface cluster configurations of gold and iron oxide increased the charge transfer and vibrational signals. The increase in the PVA-CH-symmetric and asymmetric vibrational signals was more pronounced at 45° incidence angle by 667% and 94%, respectively (*Figure 6f*), because of the increase in the optical beam area and path within the

patterned thin film. The increase in the vibrational signal intensity was 58% at a 20° angle (*Figure S-9a*).

The reduction in the gaps between PEG-C-GM-pi-FF chains combined with increased chain thickness also provided a dense hot spot volume and surface sites for the interface between PEG-C-GM-pi-FF droplets, leading to a broadband local field enhancement [88]. This broadband field enhancement could play a role in enhancing the absorption of the spectrally distributed vibrational bands [84]. The gold-iron oxide NPs interface provides an enhanced local electric field when in proximity with another, especially where the cluster is denser with little gaps between particles, as seen in gold assemblies [90]. Band CA-CO and PVA-CO also responded to the trend of chain thickness for all incident angles, where they had approximately the same vibration signal intensities at both 20° and 45° (*Figure 6e&f*). At 20° incident angle, the change in CA-CO and PVA-CO vibrational signals from CT=1.01µm to 2.82µm was 16% and 17% respectively. At 45° incident angle, this decreased by 39% for PVA-CO and increased by 19% for CA-CO under the same range. Meanwhile, at 20°, this decreased by 22% for PVA-CO and decreased by 16% for CA-CO within the same range. This was because of the absorption value at these bands for a single-layer PVA film, which was the same as the value at r=0 mm (*Figure S-9b*). However, there was a noticeable decrease in the intensity of the peaks at lower CT/CG values (*Figure S9c*).

3.4.1.4 Grazing angle Optimisation

The increase in the grazing angle improves the interaction of light with the thin film owing to spatial extension but decreases the optical density. While increased spatial extension enhances the vibration signals, decreased optical density reduces the detection sensitivity. The vibrational signal intensities were highest in the spectra obtained at 45° grazing angle (*Figure 6f*) and lowest at 82° grazing (*Figure S-9c*). At 45°, the optical density and spatial coverage of the PEG-C-GM-pi-FF chains were optimized to obtain the highest vibrational signals. These angles may be particular to the geometry of the thin film generated in this study because the greater grazing angle on the chains with a given height might cast a shadow of one strip on to the other, limiting the overall exposure of light on the material [91]. Another possibility is that incident wave backscattering increases at greater grazing angles [92]. Therefore, the optical waves interacted poorly with the thin-film pattern and glanced at the highest grazing angle. Overall, magnetically directed self-

assembly established near- and far-field interactions through good dispersion, providing tunability [93].

3.5 CONCLUSION

This study demonstrates the utilization of magnetic directed spin-coating self-assembly (MDSCSA) to fabricate an optically sensitive film consisting of periodic nanoarrays of gold nanoparticle-stabilized Pickering ferrofluid emulsion chains in PVA on a silica glass substrate. The variation in the chain thickness (CT) and gaps (CG) between the chains enhances the vibrational signal of the CH₂ infrared absorption bands. The enhancement in the CT/CG ratio from 0.11 to 2.87 resulted in a 667% increase in the infrared vibration signal of the CH₂ (2918 cm⁻¹) bond (in comparison to 2841 cm⁻¹) at 45° beam incidence, while the vibrational signals dropped at a 20° angle. These results suggest the potential of using gold nanoparticles with Fe₃O₄ to create tunable infrared resonant peak strips for surface-enhanced infrared spectroscopy. The structure of this film combines both far- and near-field effects to locally enhance the charge and vibration of the attached molecules. The variability in the resolution of a single thin film allows for greater flexibility in identifying and comprehending species traits under varying CT/CG patterns. Future work will involve investigating the minimum quantity of gold nanoparticles required in relation to Fe₃O₄ nanoparticles to establish both near-UV and near-infrared plasmon effects.

4 References

- [1] T. G. Henares, F. Mizutani, and H. Hisamoto, Current development in microfluidic immunosensing chip, *Anal. Chim. Acta* 611(1), (2008) 17-30.
- [2] S. Dehghani, R. Nosrati, M. Yousefi, A. Nezami, F. Soltani, S. M. Taghdisi, K. Abnous, M. Alibolandi, and M. Ramezani, Aptamer-based biosensors and nanosensors for the detection of vascular endothelial growth factor (VEGF): A review, *Biosens and Bioelectron.* 110 (2018) 23-37.
- [3] W. Robert J., H. Wei, P.F. Cheryl Wong, K. Ai Leen, G. Richard S. and E. M. Christopher, Formation and Properties of Magnetic Chains for 100nm nanoparticles used in separation of molecules and cells, *J. Magn. Magn. Matter*, 321(10) (2009) 1452-1458.
- [4] Z. Lu and Y. Yadong, Colloidal nanoparticle clusters: functional materials by design, *Chem. Soc. Rev.* 41(21) (2012) 6874-6887.
- [5] Y. Zhijie, W. Jingjing, G. Konrad, S. Myung-Geun and G. Bartosz, Interference-like patterns of static magnetic fields imprinted into polymer/nanoparticle composites, *Nature comms.* 8 (1) (2017) 1-8.
- [6] Z. Li, J. N. Bradely and D. Lixin, *Magnetic-Field-Based Self-Assembly*, Springer, Dordrecht, 2012.
- [7] G. Jianping, H. Yongxing and Y. Yadong, Highly Tunable Supramagnetic Colloidal Photonic Crystals, *Angew Chem Comm.* 46 (39) (2007).
- [8] J. Ge, L. He, J. Goebi and Y. Yin, Magnetically Tunable photonic Crystals in non-Polar solvents, *J. Am. Soc.*, 131(10) (2009) 3484-3488.
- [9] J. Henderson, J. Shi, S. Cakmaktepe and T. M. Crawford Pattern transfer nano manufacturing using magnetic recording for programmed nanoparticle assembly, *Nanotechnology* 23(18) (2012) 185304.
- [10] H. Kuo-Feng, L. Jung-Wwei, H. C Heng-Yu, W. Liang-Wei, H. Yen-Chun, W. Wei-Chih, C. Mu-Tung, L. Shen-Chuan, Y. Jun, I. Hsiu-Hau and L. Chih-Huang, Magnetic patterning: local manipulation of the intergranular exchange coupling via grain boundary engineering, *Scientific Reports* 5 (11904) (2015).
- [11] H. Herb, B. Christopher J. and L. William E., *Ferrofluid-based microchip pump and valve*, *Sensors and Actuators B* 99(2-3) (2004) 592-600.
(a) G. Fu, D. Huo, I. Shyha, K. Pancholi, B. Alzahrani., Experimental investigation on micromachining of epoxy/graphene nano platelet nanocomposites. *Int J Adv Manuf Technol* 107, 3169–3183 (2020). <https://doi.org/10.1007/s00170-020-05190-4>
- [12] J. Philip, T.J. Kumar, P. Kalyanasundaram and B. Raj, *Meas. Sci. Technol.*, 14 (8) (2003) 1289–1294.
- [13] H. Le, M. Wang, Q. Zhang, Y. Lu and Y. Yadong, Magnetic Assembly and patterning of General Nanoscale Materials through Nonmagnetic Templates., *Nano Lett.*, 13 (1) (2013) 264-271.
- [14] B. B. Yellen, H. Ondrej and F. Gary, Arranging matter by magnetic nanoparticle assembler, *PNAS* 102(25) (2005) 8860-8864.

- [15] G. Srinivasan, G. Sreenivasulu, C. Benoit, V.M.Petrov and F.Chavez, *J. Appl. Phys.* 117(17) (2015) 17B904.
- [16] Fiabane, J., Prentice, P. Pancholi, Ketan. (2016). High yielding microbubble production method. *BioMed Res. Intl.*, (2016), 10.1155/2016/3572827, Article ID 3572827
 (a) K. Pancholi, P.K. Robertson, P. Okpozo, N.S. Beattie, D. Huo, Observation of stimulated emission from Rhodamine 6G-polymer aggregate adsorbed at foam interfaces, *J. Phys.: Energy*, 1 (1) (2018), Article 015007
- [17] A. Claire, B. Mohamed, T. Nicolas, F. Elias, A. Florence and H. Nicolas, Pickering emulsions: Preparation processes, key parameters governing their properties and potential for pharmaceutical applications, *J. Control. Release*, 309 (2019) 302-332.
- [18] C. Kurdak, J. Kim, L. Farina, K. M. Lewis, X. Bai, M. Rowe and A. Matzger, Au Nanoparticle Clusters: A New System to Model Hopping Conduction, *Turkish journal of Phys.* 23 (2003) 419-426.
- [19] D. Luchao, X.S.Z. Guirong and F. Akihiro, Plasmon induced charge transfer mechanism in gold-TiO₂ nanoparticle systems: The size effect of gold nanoparticle, *J. Appl. Phys.* 128 (2020) 213104.
- [20] X.L.M. Bowei, Z. Junming and L. Linhua, Dependent absorption property of nanoparticle clusters: an investigation of the competing effects in the near field., *Optics Exp.* 27 8 (2019).
- [21] X. Fan, W. Zheng and D. J. Singh, Light scattering and surface plasmons on small spherical particles, *Light: Sci. Appl.* 3, (2014) e179.
- [22] S. Jingyu, T. Feng, L. Jing and Y. Mo, Nanoparticle based fluorescence resonance energy transfer (FRET) for biosensing applications, *J.Mate. Chem. B*, 35 (3) (2015) 6989-7005.
- [23] O. Eunkeu, H. Alan L., S. Andrew, E. Alexander, C. Marc, S. Kimihiro, B. Konrad, G. Ramasis, F. Fredrik K. and M. Igor L., Energy Transfer Sensitization of Luminescent Gold Nanoclusters: More than Just the Classical Förster Mechanism, *Scientific Reports, Nature*, 3 (2016) 35538.
- [24] C. George, A. Genovese, F. Qiao, K. Korobchevskaya, A. Comin, A. Falqui, S. Marras, A. Roig, Y. Zhang, R. Krahn, L. Manna, Optical and electrical properties of colloidal (spherical Au)-(spinel ferrite nanorod) heterostructures. *Nanoscale*, 3(11), (2011) 4647-4654.
- [25] A. Comin, K. Korobchevskaya, C. George, A. Diaspro, L. Manna, Plasmon bleaching dynamics in colloidal gold-iron oxide nanocrystal heterodimers. *Nano letters*, 12(2) (2012) 921-926.
- [26] W. Robert J., H. Wei, P. F. C. Wong, K. A. Leen, G. Richard and E. Christopher M Formation and Properties of Magnetic Chains for 100nm nanoparticles used in separation of molecules and cells, *J. Magn. Magn. Matter*, 321 (10) (2009) 1452-1458.
- [27] O. Alexey and Z. Andrey, Chain formation and Phase separation in ferrofluid: The influence of viscous properties, *Materials*, 13(3956) (2020).
- [28] S. Ryan, B. Jason, C. Kevin and K. Alamgir, Imaging magnetic flux lines with iron oxide nanoparticles using a fossilized liquid assembly, *Soft Matter*, 7(12) (2011) 5756-5763.
- [29] Z. Zhihan, L. Guojun and H. Dehui, Coating and Structural Locking of Dipolar Chains of Cobalt Nanoparticles, *ACS Nano*, 3(1) (2009) 165-172.

- [30] M. Samir, L. R. Damien, A. Marie-Charlotte, L. Joël and D. Véronique, Arrays of high aspect ratio magnetic microstructures for large trapping throughput in lab-on-chip systems, *Microfluid. Nanofluid.*, 22(10) (2018).
- [31] F. Leal-Calderon, T. Stora, M. O. Monval, P. Poulin and J. Bibette, Direct measurement of colloidal forces, *Phys. Rev.Lett.*72(18) (1994) 2959-2964.
- [32] F. Leal-Calderon, S. Veronique and B. Jerome, *Emulsion science: Basic principles*, New York: Springer Science and Business Media (2007).
- [33] T. Conceicao, N. Scharnagl, C. Blawert, W. Dietzel and K. Kainer, Corrosion protection of magnesium alloy AZ31 sheets by spin coating process with poly(ether imide), *Corros. Sci.*, 52(6) (2010) 2066-2079.
- [34] S. Walheim, E. Schaffer, J. Mlynek and U. Steiner, Nanophase-separated polymer films as high-performance antireflection coatings, *Science*, 283(5401) (1999) 520-522.
- [35] H. Sirringhaus, T. Nir and H. F. Richard, Integrated optoelectronics devices based on conjugate polymers, *Science*, 5370(280) (1998) 1741-1744.
- [36] K. Eaton and P. Douglas, Effect of humidity on the response characteristics of luminescent PtOEP thin film optical oxygen sensors, *Sens. and Actuators B*, 82(1) (2002) 94-104.
- [37] W. Mingsheng, G. Chuanbo, H. Le, L. Qipeng, Z. Jinzhong, T. Chi, S. Zorba and Y. Yadong, Magnetic Tuning Plasmonic Excitation of Gold Nanorods, *J. Am. Chem. Soc.*, 135(41) (2013) 15302-15305.
- [38] H. Zhang, F. Kin-Hung, H. Jürgen, C. Che Ting and W. Dayang, Controlled chainlike agglomeration of charged gold nanoparticles via a deliberate interaction balance, *The J Phys. Chem. C*, 112(14) (2008)16830-16839.
- [39] H. Chen, L. Shao, Q. Li and J. Wang, Gold nanorods and their plasmonic properties, *Chem. Soc. Rev.* 42(7) (2013) 2679-2724.
- [40] C.W. Lai, F.W. Low, M.F. Tai and S. B. A. Hamid, Iron oxide nanoparticles decorated Oleic acid for high colloidal stability, *Adv. Polym. Technol.*, 37 (2017) 1712-1721.
- [41] P. Okpozo, K. Pancholi, Study of spatial organisation of magnetic field directed gold-pickering-ferrofluid-nanoemulsion in spin coated film. *Hyb. Adv.*, (2023) 100018. <https://doi.org/10.1016/j.hybadv.2023.100018>
- [42] P. Berger, N.B. Adelman, K.J. Beckman, D.J. Campbell, A.B. Ellis, G.C. Lisensky, Preparation and properties of an aqueous ferrofluid, *J. Chem. Edu.* (1999) 943-948.
- [43] I. Hussain, M. Brust, A.J. Papworth and A.I. Cooper, Preparation of Acrylate-Stabilized Gold and Silver Hydrosols and Gold-Polymer Composite Films, *Langmuir*, 19(11) (2003) 4831-4835.
- [44] Y. Wang, J. Enrico, T. Ono, M. Maeki, M. Tokeshi, T. Isono, K. Tajima, T. Satoh, S. Sato, Y. Miura and T. Yamamoto, Enhanced dispersion stability of gold nanoparticles by the physisorption of cyclic poly (ethylene glycol). *Nature Comm.* 11(1) (2020) 1-12.
- [45] M. Hu, X. Du, G. Liu, Y. Huang, Z. Liu, S. Sun and Y. Li, Oppositely charged Pickering emulsion co-stabilized by chitin nanoparticles and fucoidan: Influence of environmental stresses on stability and antioxidant activity, *Foods*, 11(13), (2022) 1835.
- [46] Liu, H., Hou, P., Zhang, W., Kim, Y.K. and Wu, J., The synthesis and characterization of polymer-coated FeAu multifunctional nanoparticles, *Nanotechnology*, 21(33) (2010) 335602.
- [47] G.Frens, Controlled Nucleation for the Regulation of the Particle Size in Monodisperse Gold Suspensions, *Nature*, 241 (1973) 20-22.

- [48] J.Reguera, D.J. de Aberasturi, N. Winckelmans, J. Langer, S. Bals, L.M. Liz-Marzán., Synthesis of Janus plasmonic–magnetic, star–sphere nanoparticles, and their application in SERS detection, *Faraday Discuss.*, 191 (2016) 47-59.
- [49] T. Nguyen, F.Mammeri and S. Ammar, Iron Oxide and Gold Mased Magneto-Plasmonic nanostructures for Medical Applications: A Review, *Nanomaterials*, 8(149) (2018) 1-29.
- [50] M. Bajaj, N.Wangoo, D.V.S.Jainn and R. K. Sharma, Quantification of adsorbed and dangling citrate ions on gold nanoparticle surface using thermogravimetric analysis, *Scientific Report* 10(1), (2020)1-7.
- [51] M. Brugnara, Contact_Angle Image J NIH.GOV. [Online] Available at: <https://imagej.nih.gov/ij/plugins/contact-angle.html> [Accessed 27 October 2020].
- [52] A.Stalder, T. Melchior, M. Müller, D. Sage, T. Blu, M. Unser, Low-bond axisymmetric drop shape analysis for surface tension and contact angle measurements of sessile drops, *Colloids and Surf. A* 364(1-3) (2010) 72-81.
- [53] R.Chantrell, J.Popplewell and S. Charles, Measurements of particle size distribution parameters in ferrofluids, *IEEE Trans. Magn.*, 14(5) (1978) 975-977.
- [54] K. O'grady, M. El-Hilo and R.Chantrell, The characterisation of interaction effects in fine particle systems, *IEEE Trans. Magn.*, 29(6) (1993) 2608-2613.
- [55] Z. Ling, H. Rong and G. Hong-Chen, Oleic acid coating on the monodisperse magnetite nanoparticles, *Appl.Sur.Sci.*253(5) (2006) 2611-2617.
- [56] J. Ibarra, J. Melendres, M. Almada, M.G. Burboa, P. Taboada, J. Juárez, M.A. Valdez, Synthesis and characterization of magnetite/PGLA/Chitosan nanoparticles, *Mater.Res. Exp.* 2 (2015) 095010.
- [57] P. Burnham, N. Dollahon, C.H. Li, A.J. Viescas, G.C. Papaefthymiou, Magnetization and Specific Absorption Rate Studies of Ball-milled Iron Oxide Nanoparticles for Biomedicine, *J. Nanoparticles* (2013) 181820.
- [58] F.Ahangaran, A.Hassanzadeh, and S. Nouri, Surface modification of Fe₃O₄@SiO₂ microsphere by silane coupling agent, *Int.Nano. Lett.*, 3(23) (2013).
- [59] A.Filopoulou, S.Vlachou and S.C. Boyatzis, Fatty Acids and Their Metal salts: A Review of their Infrared spectra in light of their presence in cultural heritage, *Molecules*, 26(6005) (2021).
- [60] D.S. Noorsaiyyidah, C.L. N. Akmal, J. M. Rafie and R. Ahmad, FTIR Studies on Silver-Poly(Methylmethacrylate) Nanocomposites via In-Situ Polymerization Technique, *Int. J. Electrochem.Sci.*, (2012) 5596-5603.
- [61] M.Abyaneh, R.Pasricha, S. Gosavi and S.Kulkarni, Thermally assisted semiconductor-like to insulator transition in gold–poly (methyl methacrylate) nanocomposites, *Nanotechnology*, 17(16) (2006) 4129.
- [62] I.S. Mehdihasan, D.M. Patel, N. N. Patel, U. S. Patel, K. P. Patel, and R. M. Patel, Methacrylate copolymers and their composites with nano-CdS: Synthesis, characterization, thermal behavior, and antimicrobial properties. *Int. J. Indust. Chem.*, 9 (2018) 153-166.
- [63] G. Duan, C. Zhang, A. Li, X. Yang, L. Lu and X. Wang, Preparation and characterization of mesoporous zirconia made by using a poly (methyl methacrylate) template. *Nanoscale Res. Lett.*, 3(3) (2008) 118-122.
- [64] Z.Chang, Y. Xu, X. Zhao, Q. Zhang and D. Chen, Grafting poly (methyl methacrylate) onto polyimide nanofibers via “click” reaction. *ACS Appl. Mater. Interfaces*, 1(12) (2009) 2804-2811.

- [65] M.Giuliani, W.Gonzalez-Vinas, K.M.Poduska and A.Yethira, Dynamics of crystals structure formation in spin coated colloidal films, *J. Phys. Chem. Lett.*, 1(9) (2010) 1481-1486.
- [66] D.Bora, E.A. Rozhkova, K. Schrantz, P.P. Wyss, A. Braun, T. Graule and E.C. Constable, Functionalization of Nanostructured Hematite Thin-Film Electrodes with the Light-Harvesting Membrane Protein C-Phycocyanin Yields an Enhanced Photocurrent, *Adv. Func.Mater.* 22(3) (2012) 490-502.
- [67] N.Dahal and V.Chikan, Synthesis of Water-Soluble Iron-Gold Alloy Nanoparticles. *Chem. Mater.*, 20(20) (2008) 6389-6395.
- [68] E.Thimsen, F.Le Formal, M.Grätzel and S. C.Warren Influence of Plasmonic Au Nanoparticles on the Photoactivity of Fe₂O₃ Electrodes for Water Splitting, *Nano Letters*, 11(1) (2011) 35-43.
- [69] D.Sherman and T.Waite, Electronic spectra of Fe³⁺ oxides and oxide hydroxides in the near IR to near UV, *Ame.Mineralogist*, 70(11-12) (1985) 1262-1269.
- [70] V.Velasco, L. Muñoz, E. Mazarío, N. Menéndez, P. Herrasti, A. Hernando and P. Crespo Chemically Synthesised Au-Fe₃O₄ nanostructures with controlled optical and magnetic properties. *J. Phys. D: Appl. Phys.* 48 (2015) 11.
- [71] S.Mizuno, and H.Yao, On the electronic transitions of α -Fe₂O₃ hematite nanoparticles with different size and morphology: Analysis by simultaneous deconvolution of UV–vis absorption and MCD spectra, *J. Mag. Mag. Mater.* 517 (2021)167389.
- [72] T. Ung, L. M.Liz-Marzan and P.Mulvaney, Gold nanoparticle thin films. *Colloids and Surfaces A*, 202 (2002) 119-126.
- [73] I.Thomann, B.A. Pinaud, Z. Chen, B.M. Clemens, T.F. Jaramillo and M.L. Brongersma, Plasmon enhanced solar-to-fuel energy conversion. *Nano Letters*, 11(8) (2011) 3440-3446.
- [74] Y.Ye, T. P.Chen, Z.Liu, and X.Yuan, Effect of Surface Scattering of Electrons on Ratios of Optical Absorption and Scattering to Extinction of Gold Nanoshell. *Nanoscale Research Letters*, 13(229) (2018) 1-11.
- [75] J.Bhattacharai, D. Neupane, B. Nepal, M.D. Alharthi, A.V. Demchenko and K.J. Stine, Adhesion layer-free attachment of gold on silicon wafer and its application in localized surface plasmon resonance-based biosensing. *Sensors and Actuators A: Physical*, 312 (2020) 112-155.
- [76] L.Bossard-Giannesini, H.Cruguel, E.Lacaze and O. Pluchery, Plasmonic properties of gold nanoparticles on silicon substrates: Understanding Fano-like spectra observed in reflection. *Appl.Phys.Lett.* 109(11) (2016) 111901.
- [77] C.Engelbrekt, Y.Gargasya, and M. Law, Silica shell growth on Vitreophobic Gold Nanoparticles Probed by Plasmon Resonance Dynamics. *J. Phys. Chem.* 125(45) (2021) 25119-25125.
- [78] L.Liz-Marzán, Tailoring surface plasmons through the morphology and assembly of metal nanoparticles. *Langmuir*, 22(1) (2006) 32-41.
- [79] S.K. Ghosh, and T. Pal, Interparticle Coupling Effect on the Surface Plasmon Resonance of Gold Nanoparticles: From Theory to Applications. *Chem. Rev.* 107(11) (2007) 4797-4862.
- [80] L.Wang, T.Nakajima and Y.Zhang, Simultaneous reduction of surface, bulk, and interface recombination for Au nanoparticle-embedded hematite nanorod photoanodes toward efficient water splitting, *J. Mater. Chem. A* 7 (2019) 5258-5265.

- [81] J. Wilcoxon and B. Abrams, Synthesis, structure and properties of metal nanoclusters, *Chem. Soc. Rev.* 35(11) (2006) 1162-1194.
- [82] L. Wang, L. Wang, J. Luo, Q. Fan, M. Suzuki, I. Suzuki, M.H. Engelhard, Y. Lin, N. Kim, J.Q. Wang and C.J. Zhong, Monodispersed core-shell $\text{Fe}_3\text{O}_4@ \text{Au}$ nanoparticles. *The Journal of Physical Chemistry B*, 109(46) (2005) 21593-21601.
- [83] K. Korobchevskaya, C. George, A. Diaspro, L. Manna, R. Cingolani and A. Comin,, Ultrafast carrier dynamics in gold/iron-oxide nanocrystal heterodimers. *Appl. Phys. Lett.* 99(1) (2011) 011907.
- [84] T. Maß, V. Nguyen, U. Schnakenberg and T. Taubner, Tailoring grating strip widths for optimizing infrared absorption signals of an adsorbed molecular monolayer. *Optics Exp.* 27(8) (2019) 10524-10532.
- [85] T. Wang, V.H. Nguyen, A. Buchenauer, U. Schnakenberg and T. Taubner, Surface enhanced infrared spectroscopy with gold strip gratings. *Optics Exp.* 21(7) (2013) 9005-9010.
- [86] E. Blout, and R. Karplus, The infrared spectrum of polyvinyl alcohol, *J. Am. Chem. Soc.* 70(2) (1948) 862-864.
- [87] A. Wexler, Integrated Intensities of Absorption Bands in Infrared Spectroscopy, *Appl. Spectro. Rev.* 1(1) (1967) 29-98.
- [88] S. Mahendia, A.K. Tomar, R.P. Chahal, P. Goyal and S. Kumar, Optical and Structural properties of poly(vinyl alcohol) films embedded with citrate-stabilized gold nanoparticles. *J. Phys. D*, 44 (2011) 8.
- [89] M. Moreno, R. Hernandez & D. Lopez, Crosslinking of poly(vinyl alcohol) using functionalized gold nanoparticles. *European Polymer Journal*, 46 (2010) 2099-2104.
- [90] H. Ghosh and T. Burgi, Mapping Infrared Enhancement around Gold Nanoparticles Using Polyelectrolytes, *J. Phys. Chem.* 121 (2017) 2355-2363.
- [91] I. Saini, A. Sharma, N. Chandak, S. Aggarwal and P. Sharma, Ag nanoparticles induced modification in microhardness of polyvinyl alcohol, *Adv. Mater. Proc.* 3(8) (2018) 508-511.
- [92] M. Hawkeye Glancing angle deposition: Fabrication, properties, and applications of micro- and nanostructured thin films, *J. Vacuum Sci. Tech. A* 25(5) (2007).
- [93] R. Gupta, P. Gupta, C. Footer, G. B. Stenning, J. A. Darr, and K. Pancholi, Tuneable magnetic nanocomposites for remote self-healing, *Scientific Reports* (2002).